

Measurement of land surface temperature from oblique angle airborne thermal camera observations

Ryan A. E. Byerlay, Manoj K. Nambiar, Amir Nazem, Md. Rafsan Nahian, Mohammad Biglarbegian & Amir A. Aliabadi

To cite this article: Ryan A. E. Byerlay, Manoj K. Nambiar, Amir Nazem, Md. Rafsan Nahian, Mohammad Biglarbegian & Amir A. Aliabadi (2020) Measurement of land surface temperature from oblique angle airborne thermal camera observations, International Journal of Remote Sensing, 41:8, 3119-3146, DOI: [10.1080/01431161.2019.1699672](https://doi.org/10.1080/01431161.2019.1699672)

To link to this article: <https://doi.org/10.1080/01431161.2019.1699672>



Published online: 25 Dec 2019.



Submit your article to this journal [↗](#)



View related articles [↗](#)



View Crossmark data [↗](#)



Measurement of land surface temperature from oblique angle airborne thermal camera observations

Ryan A. E. Byerlay, Manoj K. Nambiar, Amir Nazem, Md. Rafsan Nahian, Mohammad Biglarbegian and Amir A. Aliabadi 

School of Engineering, University of Guelph, Guelph, Ontario, Canada

ABSTRACT

This paper presents a novel airborne remote sensing method using thermal imaging to directly georeference and calculate Earth surface temperature with a high spatiotemporal resolution. A tethered balloon is used to elevate an uncooled thermal camera in the field. When deployed, images with oblique view angles of the surrounding Earth surface are collected. Images recorded from a field environmental monitoring campaign in a northern Canadian mining facility are processed with open source software, and it is shown that they successfully represent the diurnal and spatial surface temperature variations within the facility. Furthermore, in comparison to MODerate resolution Imaging Spectroradiometer (MODIS) satellite images, the approach results in a median absolute error of 0.64 K, with a bias and Root Mean Square Error (RMSE) of 0.5 K and 5.45 K, respectively.

ARTICLE HISTORY

Received 13 May 2019

Accepted 22 November 2019

1. Introduction

1.1. Literature review

Earth surface temperature, otherwise known as Skin Temperature (ST), is an important geophysical variable that has been measured with remote sensing technologies since the 1970s (Patel (2006); Mildrexler, Zhao, and Running (2011)). Accurate quantification of ST is important for many Earth system models, including meteorological, climate, and planetary boundary layer models (Reichle et al. (2010); Tomlinson et al. (2011); Malbêteau et al. (2018)). Micro-, meso-, and macro-scale climate models all consider ST as a key variable, as noted by Gémes, Tobak, and van Leeuwen (2016). Land surface temperature is a key variable when quantifying the impacts of urban heat islands. Specifically, the diurnal impact of ST with respect to the surrounding environment is of importance to many researchers (Kawai and Wada (2007); Mathew, Khandelwal, and Kaul (2018)). Furthermore, macro- and meso-scale models, including those that model the change of climate, consider ST over both land and waterbodies as a boundary condition (Horrocks et al. (2003); Fang et al. (2018)). The impact of ST on large freshwater lakes has also been studied as surface water temperature influences thermal stratification in lakes (Kolodochka (2003); Moukomla and Blanken

(2016)). ST can be quantified as a function of Long Wave Infrared Radiation (LWIR) emitted from the Earth's surface (Wang et al. (2005)). The emitted LWIR is an important variable when considering the Earth energy budget from incoming solar radiation (Wang et al. (2005)). Before the advent of satellites and other remote sensing platforms, multiple point sources recording either surface temperature or air temperature were used in conjunction with weighting algorithms and other Geographic Information Systems (GIS) techniques to spatially represent ST (Rahaman, Hassan, and Chowdhury (2018)). These historical methods can introduce significant inaccuracies during interpolation of the data, as a result, remote sensing tools have since been utilized to reduce these data analysis errors (Rahaman, Hassan, and Chowdhury (2018)).

Conventionally, ST has been quantified from remote sensing satellites with onboard ST sensors including the MODerate Resolution Imaging Spectroradiometer (MODIS), the Advanced Baseline Imager (ABI), the Enhanced Thematic Mapper Plus (ETM+), and the Thermal Infrared Sensor (TIRS) (Inamdar et al. (2008); Tomlinson et al. (2011)). Landsat 8 sensors which derive ST, record data within the Thermal Infrared (TIR) or LWIR spectra between 8 μm and 15 μm (van der Meer (2018)).

MODIS, located on both the Terra and Aqua satellites, records two distinct thermal images daily, approximately three hours apart at a 1 km \times 1 km spatial resolution (Crosson et al. (2012); Kumar (2014); Liu et al. (2017)). The ABI, located on the Geostationary Operational Environmental Satellite (GOES) satellites, is capable of capturing thermal images every 5 min with a spatial resolution of 2 km \times 2 km (Cintineo et al. (2016); Schmit et al. (2017)). Furthermore, Landsat satellites are capable of recording TIR images. The Landsat 7 ETM+ can capture TIR images at a spatial resolution of 60 m \times 60 m and the Landsat 8 TIRS can record TIR images at a spatial resolution of 100 m \times 100 m. Both Landsat satellites have a time resolution of 16 days (Chastain et al. (2019)).

Satellite-based sensors are unable to record ST with both a high spatial and temporal resolution (Zakšek and Oštir (2012)). With the development of small Unmanned Aerial Systems (sUASs) and the miniaturisation of thermal camera technology, airborne platforms, such as drones, kites, and blimps have been used to quantify ST with a high spatiotemporal resolution (Berni et al. (2009); Klemas (2015)). Furthermore, coupling sUAS platforms with oblique thermal imaging technology and concurrent image processing methods can result in increased ST coverage.

Recently it has become increasingly common for sUAS platforms to include thermal cameras (Colomina and Molina (2014)). Uncooled thermal cameras are most often used on sUASs as they are physically lighter, inexpensive, and require less power to operate as compared to cooled thermal cameras (Sheng et al. (2010); Ribeiro-Gomes et al. (2017); Rahaghi et al. (2019)). There are many types of sUAS devices used to deploy camera systems, including but not limited to fixed wing and multi-rotor drones, kites, blimps, and balloons (Duffy and Anderson (2016)).

Tethered balloons are another aerial platform that have several advantages as compared to conventional sUASs. Tethered balloons can be deployed for hours without changing batteries, be launched in remote and complex environments where drones are unable to fly (e.g. airports), are inexpensive relative to other sUAS platforms, and their altitude can be precisely controlled, amongst other advantages (Vierling et al. (2006)). A few studies have been completed involving thermal imaging and tethered balloons. Vierling et al. (2006) deployed a helium-filled, tethered aerostat equipped with athermal

infrared sensor, capable of lifting a payload of 78 kg and flying in a maximum wind speed greater than 11 m s^{-1} . Rahaghi et al. (2019) launched a tethered-helium-filled balloon equipped with a FLIR Tau 2 thermal camera over Lake Geneva, Switzerland, under weak wind conditions.

Airborne sUAS vectors, including drones and balloons, have been noted to be deployed in maximum wind speeds up to 10 m s^{-1} , after which sUAS performance is significantly degraded (Reintsma et al. (2018)). von Bueren et al. (2015) and Hardin et al. (2019) reported that many manufacturers claim that Unmanned Aerial Vehicles (UAVs) are capable of flying in wind speeds up to 8.3 m s^{-1} . However, Hardin et al. (2019) stated that wind speeds greater than 7 m s^{-1} can impact flight time and performance. Ren et al. (2017) noted that the DJI Phantom 4 quadcopter, a popular drone produced for the consumer market, has a maximum wind resistance speed of 10 m s^{-1} . Puliti et al. (2015) collected earth surface images from a UAV over multiple flights in wind speeds up to 7 m s^{-1} , where each flight lasted approximately 24 min. Boon, Drijfhout, and Tesfamichael (2017) used two types of UAVs (fixed wing and multi-rotor) for an environmental mapping study. Both UAVs were capable of flying in a maximum wind speed of 11.1 m s^{-1} . Rankin and Wolff (2002) used a tethered balloon during a field campaign in which the manufacturer recommended use in maximum wind speeds up to 12 m s^{-1} ; however, the blimp was not flown in wind speeds above 8 m s^{-1} . Hot-air-based balloons experience inflation and positioning difficulty in wind speeds greater than 4.17 m s^{-1} and helium-filled balloons were found to be destabilized in winds greater than 1.4 m s^{-1} as described by Aber (2004).

With advancing sUAS technology, including the integration of Inertial Measurement Units (IMUs) and Global Navigation Satellite System (GNSS) units, sUAS imaging systems have been able to directly georeference images without the use of ground control (Colomina and Molina (2014); Stöcker et al. (2017); Padró et al. (2019)). The angular and positioning data provided by these systems can either be used directly or processed with Real-Time Kinematic (RTK), Post-Processing Kinematic (PPK), Precise Point Positioning (PPP), or differential correction techniques prior to being utilized in direct georeferencing methods (Moen, Pastor, and Cohen (1997); Zhang, Guo, and Li (2012); Bakula et al. (2017); Stöcker et al. (2017)). Without the use of differential correction for geographical coordinates calculated from direct georeferencing, positional accuracy in the range of 2–5 m is typical (Turner, Lucieer, and Wallace (2014); Whitehead et al. (2014)). Padró et al. (2019) quantified Root Mean Square Error (RMSE) for GNSS direct georeferencing without correction and PPK methods with respect to pre-defined ground control point locations. Planimetric RMSE for the uncorrected GNSS direct georeferenced data was 1.06 m, while vertical error was 4.21 m. The RMSE for the PPK methods were at least one order of magnitude less than that of the uncorrected direct georeferencing method. However, Padró et al. (2019) noted that the uncorrected GNSS approach may be appropriate, such as in cases of analysing satellite images with pixel size of greater than 2 m.

Thermal cameras use microbolometer focal plane arrays to observe incoming radiant energy (FLIR-Systems (2012); Olbrycht and Więcek (2015)). When an image is captured, the microbolometer array represents the observed energy as a signal value (commonly referred to as digital numbers or A/D counts) which includes the radiant energy emitted from the atmosphere, reflected by the surface, and recorded from the imaged surface of the object (Zeise, Kleinschmidt, and Wagner (2015)). Microbolometer temperature is

known to vary as a function of sensor, camera, and ambient temperatures (FLIR-Systems (2012); Budzier and Gerlach (2015); Lin et al. (2018)). Cooled thermal cameras are significantly more sensitive than uncooled systems and provide more accurate absolute temperatures (Ribeiro-Gomes et al. (2017)). However, current cooled camera technology requires an airborne vector capable of lifting more than 4 kg, which is greater than the capacity of sUAS and smaller tethered-balloon-system payloads (Torres-Rua (2017)). It has been noted in literature that uncooled thermal cameras can be radiometrically calibrated to reduce uncooled camera error to ± 5 K (Gallardo-Saavedra, Hernández-Callejo, and Duque-Perez (2018); Kelly et al. (2019)).

Oblique imaging systems coupled with sUAS or tethered-balloon systems can significantly increase the recorded land surface area as compared to nadir imaging systems. However, radiometric thermal imaging systems can be impacted by non-nadir setups, where surface temperature error is introduced as a function of observation angle (Dugdale (2016)). Viewing angles greater than 30° of nadir over waterbodies have been noted to introduce surface temperature error of approximately 0.5 K (Torgersen et al. (2001); Kay et al. (2005); Dugdale (2016)). This error is introduced as the surface emissivity of water changes as the viewing angle of the thermal camera becomes more oblique and reflected radiation from the surface increasingly influences the thermal camera internal sensor (Dugdale (2016)). Horton et al. (2017) noted that sea surface temperature emissivity varied between 0.36 and 0.98 for viewing angles between 90° (nadir) and 5° (below horizontal), respectively. James et al. (2006) recorded ground-based oblique thermal images of lava flows and quantified a $\pm 3\%$ difference in radiative power from the lava flows where error increases as more distant objects had high emissivities as compared to closer ones. More distant objects were likely to be influenced the most by increasingly oblique viewing angles. In the study, they accounted for atmospheric transmission effects of the radiation (James et al. (2006)). Hopskinson et al. (2010) recorded ground-based oblique thermal images of a glacier at varying diurnal times. It was noted that the maximum temperature difference was ± 3 K, where the emissivity was assumed to be 0.98. However, the calculated glacier surface temperatures were not validated. As a result, it is possible that these temperature variations could be influenced by transmitted and reflected radiation.

1.2. Technology gaps

High spatial and temporal resolution data of the Earth's surface capable of characterizing diurnal ST patterns is difficult to obtain from conventional remote sensing sources (Malbêteau et al. (2018)). Furthermore, the use of open-source direct georeferencing methods and surface temperature calculation for thermal images collected from airborne vectors at oblique angles are not widely reported (Verykokou and Ioannidis (2018)). The coupling of direct georeferencing thermal images captured from a tethered-balloon-based vector is novel, and the focus of this paper is the development of an open-source image processing workflow to map surface temperatures with a high spatiotemporal resolution.

1.3. Objectives

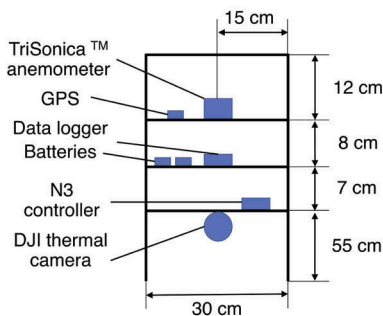
In this paper, the development of an open-source, Python-based thermal image direct georeferencing and ST calculation method is described and evaluated with respect to MODIS satellite imagery. The developed program quantifies ST at a high spatiotemporal resolution as compared to conventional satellite sources. The images were collected during an environmental monitoring field campaign conducted within a remote, northern Canadian mining facility in May 2018 (Figure 3). In total, 11,697 images were recorded. Of this total, approximately 98% of the images were used in the analysis.

Section 2 describes the instruments used in the field campaign as well as the developed imaging workflow and the picture collection procedure followed during the field campaign. Section 3 includes the plots of the geographic distribution of ST over four-hour time intervals, an absolute comparison between ST derived from the method, ST derived from a MODIS data product with respect to the mining facility, and a Principal Component Analysis (PCA) of ST spatial variation during each four-hour interval. Section 4 concludes the paper and details future work plans.

2. Methods

2.1. Experimental materials

The images processed in the paper were obtained from a DJI Zenmuse XT 19-mm lens uncooled thermal camera, which was located onboard a customized airborne platform: the Tethered And Navigated Air Blimp 2 (TANAB2). In addition to the thermal camera, a TriSonica™ anemometer, measuring wind speed, wind direction, air pressure, and air temperature at 10 Hz, a TriSonica™ datalogger, and a DJI N3 flight controller were included onboard the TANAB2. The camera, TriSonica™ system, N3, and related equipment, including batteries, were all located on the TANAB2 payload, referred to as the gondola. The layout of the instruments on the gondola, the dimensions of the gondola and the TANAB2 in flight are detailed in Figure 1.



(a)



(b)

Figure 1. (a) Diagram of the gondola on the TANAB2; (b) the TANAB2 deployed during a field environmental monitoring campaign in May 2018.

The TriSonica™ anemometer has a temperature measurement range of -40 – 80 °C with a resolution of 0.1 K and an accuracy of ± 2 K. Furthermore, the TriSonica™ anemometer has a pressure measurement range of 50 – 115 kPa with a resolution of 0.01 kPa and an accuracy of ± 1 kPa.

The DJI Zenmuse XT radiometric thermal camera with a 19 -mm lens is sensitive to radiation within the 7.5 – 13.5 μm band and has a focal plane array resolution of 640×512 (horizontal pixels by vertical pixels). The camera has a radiometric sensitivity of less than 0.05 K and an accuracy of ± 5 K. The 19 -mm lens has a horizontal field of view of 32° and a vertical field of view of 26° . The radiometric camera is also capable of recording pixel data at 14 -bit resolution.

The TANAB2 and the DJI thermal camera have been deployed and surface images have been recorded in a remote mining site in northern Canada during dawn, day, dusk, and night. All observations took place in May 2018. The TANAB2 was deployed a total of twelve times at three different locations as denoted by Figure 3. Within the boundaries of the remote mining site, the TANAB2 and DJI camera setup were used in conjunction with a Lightbridge2 controller and either an Android- or iOS-powered smartphone. With the TANAB2 deployed, using the Lightbridge2, the thermal camera was tilted parallel to the horizon and was positioned at either the left- or rightmost maximum of the camera gimbal. Methodically, the camera was panned horizontally and an image was captured approximately every 5° . When the maximum Yaw limitation of the gimbal was reached, the camera was tilted approximately every 5° towards the Earth's surface and the imaging procedure repeated again until the camera was perpendicular to the ground. This imaging procedure occurred approximately every hour during each TANAB2 launch in an effort to record the diurnal variation of surface temperature.

A typical TANAB2 deployment included the controlled release of the TANAB2 and gondola from the Earth's surface, up to a maximum altitude of 200 m above ground level. Using a manually controlled reel and rope tether, the TANAB2 was released and retrieved at a constant rate. In general, one profile and retrieval of the TANAB2 lasted a total of one hour. The maximum altitude of each specific profile varied as a function of environmental conditions. During periods of increased wind velocities, up to three mooring lines were attached to the TANAB2 and controlled by personnel on the ground. The use of mooring lines allowed the TANAB2 to be deployed in environments with a maximum wind speed of 10 m s^{-1} (see Figure 2). The addition of each rope results in a lower launch altitude (and ultimately less mapped area) due to addition of weight during periods of atmospheric instability such as the afternoons. This trade-off was deemed acceptable as it was imperative to launch the TANAB2 in both stable and unstable atmospheric conditions to successfully map diurnal surface temperatures.

The TANAB2 was launched a total of 12 times at the mining facility (Figure 3), recording approximately 50 hours of TriSonica™ data. The details of each deployment are noted in Table 1.

2.2. Method development

The Python-based image processing workflow was created using Python 3.5 on Ubuntu 16.04 and associated open-source software, including ExifTool 10.94 (<https://www.sno.phy.queensu.ca/~phil/exiftool/> (Accessed 23 September 2019)) and ImageMagick 7.0.7. (<https://>

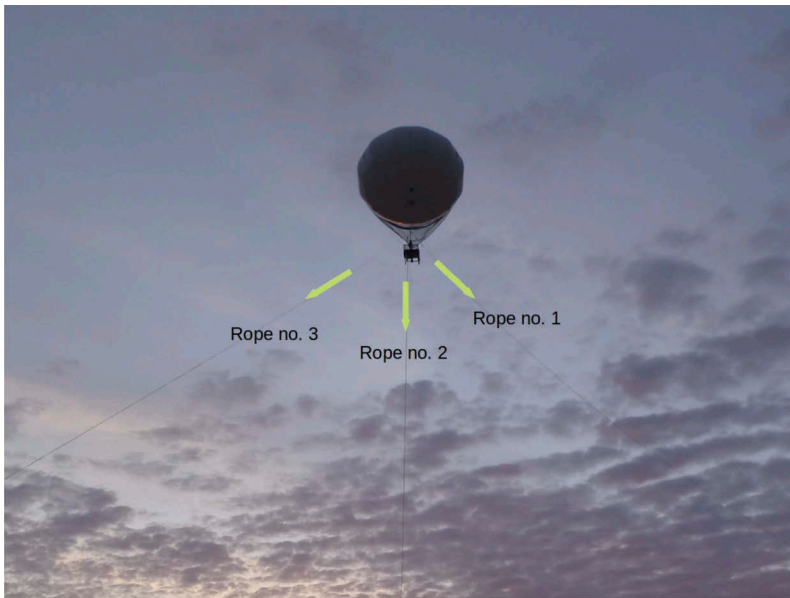


Figure 2. Use of three ropes controlled by personnel on the ground during a launch of the TANAB2 at the mining facility in May 2018.

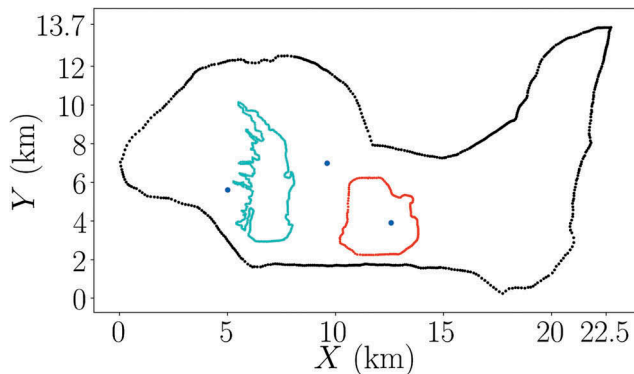


Figure 3. Diagram of the mining facility, where the black dots represent the edge of the facility, the red dots represent the outline of the mine, the teal dots represent the outline of the tailings pond, and the blue dots represent where the TANAB2 was deployed during the field environmental monitoring campaign in May 2018.

www.imagemagick.org/ (Accessed 23 September 2019)). Commands derived from these programs were executed through the Linux terminal window within the Python script. Data recorded by the integrated camera and flight controller system on the TANAB2 were stored within each image file. This data was utilized within the developed mathematical calculations.

The image processing workflow includes two general functions, one to directly georeference image pixels and the other to calculate ST from selected image pixels. These two functions will be discussed in detail separately. The process utilized to conduct the PCA of ST is also detailed.

Table 1. TANAB2 launch details; times are in Local Daylight Time (LDT).

Experiment	Location	Start date	Start time	End time	No. profiles	Duration
1	Tailings pond	7 May 2018	21:41:00	02:47:00	14	05:06:00
2	Tailings pond	9 May 2018	03:30:00	04:00:00	2	00:30:00
3	Tailings pond	10 May 2018	02:30:00	08:30:00	21	06:00:00
4	Tailings pond	15 May 2018	04:55:00	11:00:00	22	06:05:00
5	Mine	18 May 2018	04:12:00	11:12:00	20	07:00:00
6	Mine	19 May 2018	18:52:00	23:15:00	17	04:23:00
7	Mine	21 May 2018	11:00:00	12:17:00	4	01:17:00
8	Mine	23 May 2018	01:47:00	05:30:00	10	02:43:00
9	Mine	24 May 2018	11:19:00	14:25:00	12	03:06:00
10	Mine	27 May 2018	14:38:00	17:50:00	18	03:12:00
11	Tailings pond	30 May 2018	10:55:00	18:57:00	24	08:02:00
12	Tailings pond	31 May 2018	11:07:00	14:43:00	8	03:36:00

ExifTool was used to extract and assign the gondola's longitude and latitude coordinates, camera gimbal's Roll, Yaw, and Pitch angles, and gondola's Roll, Yaw, and Pitch angles, located in the metadata of each image, to variables in Python. A few images were removed from the workflow due to excessive angles of the gondola or camera. The camera Roll angle did not significantly impact the method as the Zenmuse XT was self stabilized. However, if the gondola Roll degree was greater than 45 degree or less than -45 degree, the camera became destabilized. Images with gondola Roll angles outside of this range were omitted from the workflow. Furthermore, the mechanical Pitch range of the camera was noted to be between 45° and -135°. Gimbal Pitch angles greater than 0° primarily included images of the sky, gimbal Pitch angles equivalent to 0° were images of the horizon, and gimbal Pitch angles less than 0° included images primarily of the ground. It was determined that the recorded camera gimbal Pitch angle corresponded to the Pitch angle for the middle of each image. Any images with a gimbal Pitch angle greater than or equal to -2° were omitted from the image processing analysis. Furthermore, very oblique pitch angles, greater than -30° from the horizon, were noted to possibly introduce errors into the ST calculations (FLIR-sUAS (2016)) but were not necessarily eliminated. Based on physical parameters of the camera, including the Vertical and Horizontal Fields Of View (VFOV and HFOV) angles, images with a gimbal Pitch angle less than or equivalent to -76° were also removed from the analysis. This filter was chosen because the bottom of the image would have a corresponding Pitch angle of the recorded gimbal Pitch angle, plus one half of the VFOV that would result in an angle close to or less than -89° which may disrupt direct georeferencing calculations. The Pitch angles filtered are related to the compromise between ST spatial distribution and ST accuracy because the TANAB2 only reached a maximum altitude of 200 m above ground level.

2.3. Georeferencing

As reported in literature, the Global Positioning System (GPS)-sensor-derived altitude can vary significantly up to 50 m as stated by Eynard et al. (2012). Padró et al. (2019) reported a vertical RMSE of 4.21 m for a system that used data collected from the GNSS system of the UAV used in their experiment. The TANAB2 system used the DJI N3 flight controller which includes a GNSS-Compass unit (a GPS module is included within this system). Since an accurate measurement of TANAB2 gondola altitude was required for direct georeferencing of thermal images with the developed method, the hypsometric equation was

used to calculate altitude. The hypsometric Equation (1) uses atmospheric pressure and accounts for atmospheric temperature changes within the formula (Bolanakis, Kotsis, and Laopoulos (2015); Stull (2015))

$$z_2 - z_1 \approx a \bar{T}_v \ln \left(\frac{P_1}{P_2} \right), \quad (1)$$

where z_1 and z_2 represent the altitudes (in metres) corresponding to the recorded pressure measurements (in mBar; however, the units of pressure do not affect this equation), P_1 and P_2 , \bar{T}_v represents the average virtual temperature between the two altitudes (z_1 and z_2), and a is a constant equivalent to 29.3 m K^{-1} (Stull (2015)). The uncertainty of error for Equation (1) was quantified using Equations (2–4) (Ku (1966)). A sample calculation was completed using the theory of error propagation, where P_2 is 100 kPa, P_1 is 101.3 kPa, and \bar{T}_v is 300 K. The atmospheric pressure and temperature measurements were obtained from the TriSonica™ anemometer where the pressure measurement had an uncertainty of 0.01 kPa and the temperature measurement had an uncertainty of 2 K. The uncertainty calculated was 1.2 m. Note that since differential altitude from the ground is desired, the appropriate uncertainty for the pressure is the resolution of the measurement. With this known uncertainty, this method was deemed acceptable over using the raw GPS altitude data provided by the DJI N3 flight controller unit.

$$\Delta z_2 = \sqrt{\left(\frac{\partial z_2}{\partial \bar{T}_v} \right)^2 \Delta \bar{T}_v^2 + \left(\frac{\partial z_2}{\partial P_2} \right)^2 \Delta P_2^2}, \quad (2)$$

$$\frac{\partial z_2}{\partial \bar{T}_v} = a \ln \left(\frac{P_1}{P_2} \right), \quad (3)$$

$$\frac{\partial z_2}{\partial P_2} = a \bar{T}_v \left(\frac{-1}{P_2} \right). \quad (4)$$

All recorded TriSonica™ data were averaged to the nearest whole second. For each image, the corresponding day of year in seconds was calculated and the altitude index with the smallest difference between the TriSonica™ and image day of year in seconds was selected. This altitude was referred to as the altitude in metres of the camera gimbal above ground level.

With the altitude of the camera gimbal known, trigonometric relationships were derived to calculate the geographic coordinates of the four corners, the four midpoints, and centre of each projected image on the surface of the Earth. The gimbal pitch angles for the top and bottom of each image were calculated by adding and subtracting half of the VFOV to the gimbal pitch angle, respectively. If the top pitch angle was greater than or equal to -1° , the top pitch angle was adjusted to equal -1° to ensure that all image pixels included the Earth's surface. All angles used in the georeferencing calculations were converted to radians.

In total, the TANAB2 was launched at three locations during the entire field campaign. The TANAB2 was only deployed at a maximum of one location each day. Using Google Earth, the surface elevation above sea level was calculated for each launch location at the site. Using a variation of the Haversine formula, the distance between the gondola

coordinates (lat_2 and lon_2) and each of the three launch locations (lat_1 and lon_1) were calculated, and the minimum distance was chosen, for which a base altitude from Google Earth was assigned. The distance is calculated using

$$d_{\text{launch}} = R \left[2 \tan^2 \left(\sqrt{\sin^2 \left(\frac{lat_2 - lat_1}{2} \right) + \cos(lat_1) \cos(lat_2) \sin^2 \left(\frac{lon_2 - lon_1}{2} \right)} \right) \right. \\ \left. , \sqrt{\left(1 - \left(\sin^2 \left(\frac{lat_2 - lat_1}{2} \right) + \cos(lat_1) \cos(lat_2) \sin^2 \left(\frac{lon_2 - lon_1}{2} \right) \right) \right)} \right], \quad (5)$$

where R represents the Equatorial Radius of the Earth in kilometres. The geographic location associated with the smallest value of d_{launch} was determined to be the TANAB2 deployment location. With the smallest distance known, the appropriate base altitude in metres above sea level was assigned for each image.

The direct georeferencing workflow functioned by considering surface elevation with respect to geographic distance away from each TANAB2 launch location for the eight cardinal directions (north, north-west, west, south-west, south, south-east, east, and north-east) and the line of sight from the camera for a given image pixel. Land surface elevation data in metres above sea level for the eight cardinal directions up to 10 km away from each TANAB2 deployment location were obtained from the Geocontext-Profiler (<http://www.geocontext.org/publ/2010/04/profiler/pl/>) (Accessed 23 September 2019) and saved as individual text files. The camera gimbal Yaw angles were recorded in degrees, positive clock-wise from north. If the Yaw angles were negative, 360° was added to the gimbal Yaw angle. Based on the Yaw angle of the camera gimbal and the base altitude, the appropriate file, containing data from the Geocontext-Profiler, was loaded into the Python script and a third-order polynomial was fitted to the data. Third-order models have been used to represent curved Earth surfaces (Schmidt, Evans, and Brinkmann 2003), such as those encountered in this mining facility.

The line of sight for a given image pixel was constructed by calculating the slope, which is represented by the tangent of the pitch angle. For example, for the top centre pixel, the tangent of the top pitch angle is the slope of the line of sight for the top pixel, equal to the TANAB2 altitude divided by the horizontal distance from the base of launch to where the line of sight intercepts the horizontal axis. This slope is negative because the camera's line of sight is always below horizon.

From the derived third-order polynomial for land surface elevation, the horizontal distance from the TANAB2 to where the image pixel is pointing to was determined (d_{horiz}). The roots of the intersection of the polynomial curve and the line of sight give the horizontal distance. If the roots were not real, the specific image was omitted from the ST calculation process. If multiple roots were found, the smallest real positive solution was chosen. If d_{horiz} was greater than 100 km then the pixel was omitted from the analysis.

With the horizontal distance from the TANAB2 to where the image pixel is pointing to known, the geographic coordinate pair for the corresponding horizontal (left to right) and vertical (top to bottom) pixel locations in the image were calculated using a variation of the Haversine formula

$$\text{Lat}_2 = \text{asin}[\sin(\text{Lat}_1)\cos\left(\frac{d_{\text{horiz}}}{R}\right) + \cos(\text{Lat}_1)\sin\left(\frac{d_{\text{horiz}}}{R}\right)\cos(\text{Yaw})] \quad (6)$$

$$\begin{aligned} \text{Lon}_2 = \text{Lon}_1 + \text{atan}^2([\sin(\text{Yaw})\sin\left(\frac{d_{\text{horiz}}}{R}\right)\cos(\text{Lat}_1)] \\ , [\cos\left(\frac{d_{\text{horiz}}}{R}\right) - \sin(\text{Lat}_1)\sin(\text{Lat}_2)]), \end{aligned} \quad (7)$$

where Lat_2 and Lon_2 represent the geographic coordinates for the projected image pixel pair, Lat_1 and Lon_1 represent the geographic coordinates of the TANAB2 gondola when the image was recorded, and d_{horiz} represents the horizontal distance the projected image pixel is away from the TANAB2 in kilometres. The geographic coordinates for the top centre, middle, and bottom centre of each image were calculated.

When determining the geographic coordinates for the image corners and edge mid-points, the geographic distance from the TANAB2 and the edge of the image was calculated

$$d_{\text{edge}} = \frac{d_{\text{horiz}}}{\cos(0.5\text{HFOV})}, \quad (8)$$

where d_{edge} represents the geographic distance in kilometres from the TANAB2 to the top, middle, and bottom of the projected image edge (both left and right edges), and HFOV represents the camera horizontal field of view. In total, three d_{horiz} values were used, one for pixels at the top of the image, another for pixels in the middle of the image, and one for pixels at the bottom of the image. With d_{edge} known, d_{horiz} is replaced accordingly such that geographic coordinate pairs along edges of each image can be calculated.

With the coordinate pairs of midpoints of the centre, edges, and corners of each image calculated, pixels within the image matrix were georeferenced and the corresponding ST values were calculated accordingly. For instances, where a new pitch angle for the top of the image was assigned (for images whose portion of the top needed to be eliminated), a mathematical relationship was derived to quantify which image pixel rows from the top were to be omitted from the image processing analysis.

Figure 4 provides an illustration for the angles used to correlate image pixel position to geographic coordinate location. P_0 , P_x , P_{256} , and P_{512} represent the top, the new top, the centre, and the bottom pixel rows, respectively, as each image has 640 horizontal pixels and 512 vertical pixels. Y_t , Y_{tx} , Y_c , and Y_b represent the horizontal geographic distances away from the TANAB2 for the top, new top, centre, and bottom of each image, respectively. θ represents the camera gimbal pitch angle, 13° is half of the VFOV, and γ and β are angles that are used to correlate pixels to distances using

$$\gamma = \text{atan}\left(\frac{d_{\text{horiz}_{\text{top}}}}{Z_{\text{AGL}}}\right), \quad (9)$$

$$\beta = 90^\circ - |\theta| + 0.5\text{VFOV} - \gamma, \quad (10)$$

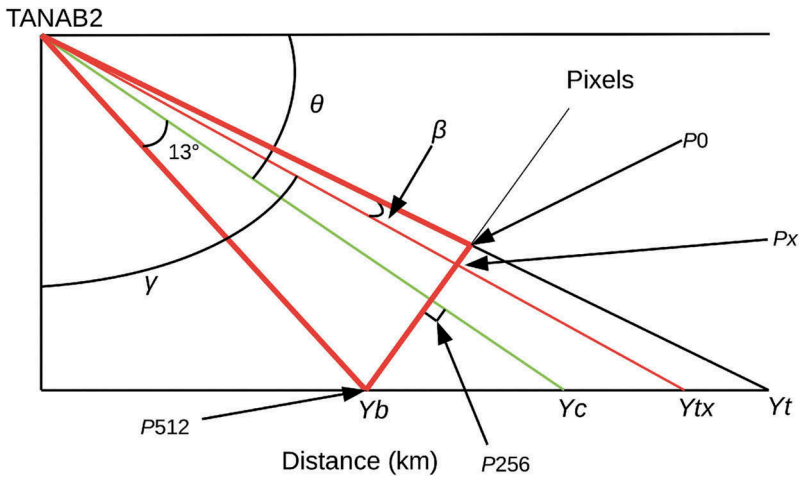


Figure 4. Relationship between pixels and horizontal geographic distances.

$$X = \frac{0.5VPR\sin(\beta)}{\sin(0.5VFOV)\sin(180^\circ - \eta)}, \tag{11}$$

where VPR is the Vertical Pixel Range (512 based on the camera specifications). Note $d_{horiz_{top}}$ is the horizontal distance that TANAB2 makes with the land location associated with the top of the image, and z_{AGL} is altitude above ground level. The new top pixel, X , was derived from Figure 5 by applying the sine law and rearranging the equation. Figure 5 displays the red triangle, illustrating the vertical camera view from the TANAB2 in greater detail. X represents the number of pixel rows to omit from the top of the image which is a function of the new top angle in the instance that the top pitch angle is greater than -1° .

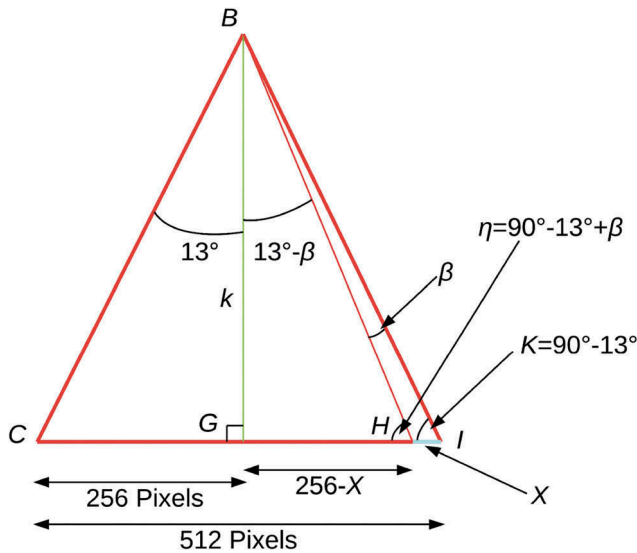


Figure 5. Relationship between vertical image pixels and the camera VFOV.

Considering all image pixels was not a possibility due to the extreme volume of computational operations required. Instead, a geometric step function was implemented to identify which pixel rows to consider for ST. This was motivated by the fact that pixels near the top of the image correspond to more land surface coverage, so they must be analysed at higher resolution. The geometric step function was achieved using the following equation and coefficients

$$y_{\text{pixel}} = 18(1.41)^n, \quad (12)$$

where n ranges from 2 to 10. The first two pixel rows to process were chosen to be 0 and 18. Equation (12) yields the corresponding pixel rows: 35, 50, 71, 100, 141, 199, 281, and 396. These rows were selected because they are densely packed in the top half of each image. The geographic distance between pixel rows at the top of an image would be greater than the geographic distance of pixel rows at the bottom of an image. To optimize processing efficiency and increase ST spatial distribution, the coefficients in Equation (12) were chosen to satisfy the desired image processing criteria. Depending upon application, this pixel row processing workflow can be changed to increase or decrease the number of pixels used in the ST calculations accordingly. The horizontal pixel step was set at a fixed value of 64. For each image, every 64th pixel column was used in the ST calculation.

When iterating through the image pixel matrix, β and γ angles were calculated for each pixel coordinate and a corresponding camera line of sight was calculated. Based on the relationship identified in [Figures 4 and 5](#), the sine law was employed in Equation (13) to derive Equation (14). The resulting slope of the camera line of sight for each pixel coordinate pair was used to relate the pixel pairs to geographic distances used to georeference pixels within the image as completed with Equations (6) and (7)

$$\frac{\sin(0.5\text{VFOV})}{\sin(\kappa)[0.5\text{VPR}]} = \frac{\sin(0.5\text{VFOV} - \beta)}{\sin(\eta)[0.5\text{VPR} - j]}, \quad (13)$$

$$\beta = -\text{atan}\left(\frac{[0.5\text{VPR} - j]\sin(0.5\text{VFOV})}{0.5\text{VPR}\sin(\kappa)}\right) + 0.5\text{VFOV}, \quad (14)$$

$$\gamma = 90^\circ - |\theta| + 0.5\text{VFOV} - \beta, \quad (15)$$

$$\text{Slope} = \frac{-1}{\tan(\gamma)}. \quad (16)$$

Here, j is the location of the pixel coordinate row from top to bottom. With the slope for the camera line of sight for a particular pixel coordinate pair known, the intersections between the third-order model representing the land surface and the pixel line of sight were derived. The smallest real positive solution was chosen to be the projected horizontal distance away from the TANAB2 for pixels located in the middle column (pixel 320 from left to right) of the image. Pixels horizontally adjacent to the centre of an image required an adjustment to the heading degree (Yaw). The offset angle (α) to apply to the heading degree was determined to be a function of the HFOV of the camera. Depending on the location of the pixel coordinate column i from left to right, the angular offset formula varied

$$\alpha_{i=0} = \frac{-\text{HFOV}}{2}, \quad (17a)$$

$$\alpha_{i>0, i<320} = \frac{-\left(\frac{\text{HPR}}{2} - i\right)\text{HFOV}}{\text{HPR}}, \quad (17b)$$

$$\alpha_{i=320} = 0, \quad (17c)$$

$$\alpha_{i>320, i<640} = \frac{\left(i - \frac{\text{HPR}}{2}\right)\text{HFOV}}{\text{HPR}}, \quad (17d)$$

$$\alpha_{i=640} = \frac{\text{HFOV}}{2}, \quad (17e)$$

where HPR represents the Horizontal Pixel Range (640 pixels based on the physical camera specifications). The Yaw heading of the camera gimbal corresponded to the middle of the image. As a result, the heading for any pixels to the left of the centre of the image required the angular offset to be removed from the recorded Yaw. Likewise, any pixels to the right of the image required the angular offset to be added to the recorded Yaw. In cases where the addition of the angular offset to the heading angle resulted in a negative value or a value greater than 2π radians, then 2π radians were either added or subtracted, respectively, to ensure that only positive angles between 0 and 2π radians were passed to Equations (6) and (7).

2.4. Surface temperature calculation

Using ExifTool and ImageMagick, recorded signal values from individual pixels were extracted and saved to a matrix in the Python script. These raw signal values were converted to surface temperatures considering a variation of Planck's Law.

Due to field conditions and physical limitations encountered at the mining facility, errors introduced from reflections and transmission could not be accounted for. However, the thermal camera used in the field campaign was calibrated in a pre-field campaign outdoors experiment on campus at the University of Guelph, Guelph, Ontario, Canada. Three radiometric images were captured roughly 30 s apart for every hour between 06:00 and 23:00 Local Daylight Time (LDT) over two consecutive days. The 30-s time interval was selected as Olbrycht and Więcek (2015) noted that uncooled thermal cameras can experience temperature drift up to 1 K per minute if a radiometric calibration was not recently completed. Four different land surface types were imaged including water, soil, grass, and developed land (urban surfaces). Each image included a certified thermometer which measured the corresponding land surface temperature as recorded by the image.

Surface temperatures from the top of the thermometer were calculated from the thermal images using FLIR Tools. For each hourly image set, the average of the surface temperatures derived in FLIR Tools was calculated and used to calibrate the R , B , O , and F constants accordingly, where $R = \frac{R_1}{R_2}$. The temperatures recorded by the certified thermometer were scaled to adjust for the test location's height above sea level (334 m for

Guelph, Ontario, Canada). For the thermal image temperatures, U_{Obj} was calculated from Equation (18).

$$U_{Obj} = \frac{R}{\exp\left(\frac{B}{T_{Obj}}\right) - F} - O, \quad (18)$$

where U_{Obj} represents the radiative energy emitted from the imaged object, T_{Obj} represents the surface temperature of the imaged object derived from FLIR Tools, R represents the uncooled camera response, B is a constant related to Planck's radiation law, F relates to the non-linear response of the thermal imaging system, and O represents an offset (Budzier and Gerlach (2015)). Equation (18) can be rearranged to calculate T_{Obj} as per Equation (19).

$$T_{Obj} = \frac{B}{\ln\left(\frac{R}{U_{Obj}+O} + F\right)}. \quad (19)$$

The R , B , O , and F constants used to calculate the U_{Obj} value were the default constants stored in the metadata of each thermal image. The default constants and calibrated constants are displayed in Table 2.

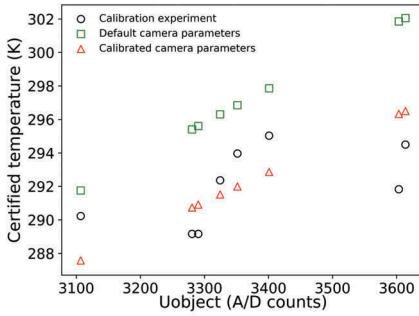
Using the empirical line method, described by Smith and Milton (1999), the U_{Obj} values and the corresponding certified thermometer temperatures were plotted against each other to calibrate the constants used in Equation (19) as a function of land surface type. The figures illustrating the empirical line method are displayed in Figure 6. The Non-Linear Least-Squares Minimization and Curve-Fitting (LMFIT) of Python library version 0.9.13 was used with Equation (19) to fit and optimize the camera constants while minimizing residuals for each specific land surface type.

Using the LMFIT library to fit camera constants for each land surface ultimately reduced the bias and RMSE values when compared to the default camera constants shown in Table 3. Using the calibrated constants for the calculation of land ST at the mining facility improved accuracy of the measurement. These findings are comparable to Gallardo-Saavedra, Hernández-Callejo, and Duque-Perez (2018) who reported that the manufacturer stated accuracy of the FLIR Vue Pro R 640, Tau 2 640, and Zenmuse XT 640 was ± 5 K. Similarly, Kelly et al. (2019) used the empirical line calibration method for a FLIR Vue Pro 640 uncooled thermal camera and quantified the accuracy of the camera to be ± 5 K.

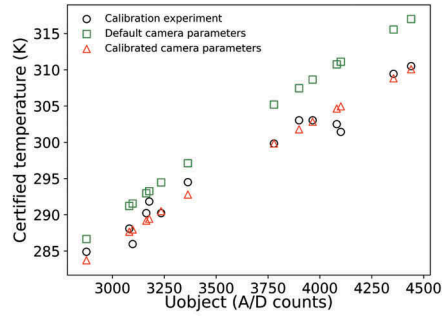
Camera constants were applied to the surfaces within the mining facility with geographical coordinates closest to the calibrated land use categories. The effect of emissivity was considered by using the BroadBand Emissivity (BBE) as described by Wang et al. (2005) and calculated in Equation (20)

Table 2. Default and calibrated camera parameters.

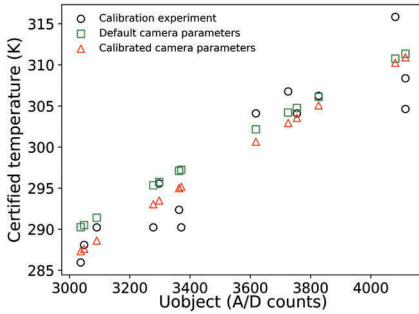
Camera parameters	R	B	O	F
Default	366,545	1428	-342	1
Calibrated water	549,789	1507	-171	1.5
Calibrated soil	549,800	1510	-171	1.5
Calibrated developed land	247,614	1322	-513	1.5
Calibrated grass	314,531	1391	-513	1.5



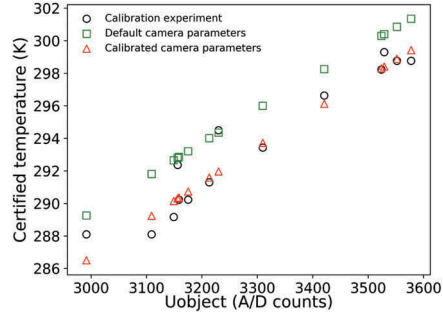
(a) Default and calibrated temperature for water.



(b) Default and calibrated temperature for soil.



(c) Default and calibrated temperature for developed land.



(d) Default and calibrated temperature for grass.

Figure 6. Certified temperature compared to radiometric image pixel signal value for water, soil, developed land, and grass.

$$BBE = a\epsilon_{29} + b\epsilon_{31} + c\epsilon_{32}, \tag{20}$$

where a , b , and c are constants that vary as functions of land surface, and ϵ_{29} , ϵ_{31} , and ϵ_{32} are emissivities derived from the MOD11B3 MODIS data product from bands 29, 31, and 32, respectively. Wang et al. (2005) determined that a , b , and c constants are similar for vegetation, soil, and anthropogenic materials. As a result, the a , b , and c coefficients were selected to be 0.2122, 0.3859, and 0.4029, respectively (Wang et al. (2005)).

The total signal (U_{Tot}) recorded by the uncooled thermal camera can be separated into three components as in Equation (21). The first component represents the radiative energy emitted from the imaged object (U_{Obj}), the second component represents the reflected energy from the imaged object (U_{Refl}), and the third component accounts for the radiative energy transmitted from the atmosphere (U_{Atm}). ϵ represents the emissivity of the surface and is accounted for by Equation (20) and τ represents the transmissivity of the atmosphere whose value is generally close to 1.0 (Usamentiaga et al. (2014)). As a result, only the radiative energy reflected and emitted from the imaged object are considered in Equation (21), where to retrieve U_{Obj} and subsequently T_{Obj} , U_{Refl} is removed from U_{Tot} . The calibration of camera constants was completed to correct for incoming reflected radiation via

$$U_{Tot} = \epsilon\tau U_{Obj} + \tau(1 - \epsilon)U_{Refl} + (1 - \tau)U_{Atm}. \tag{21}$$

Table 3. Default and calibrated camera parameter statistics.

Surface	Water	Soil	Developed land	Grass
Default bias (K)	5.18	4.81	1.83	2.07
Default RMSE (K)	5.83	5.34	3.91	2.34
Calibrated bias (K)	0.27	-0.09	0.13	-0.24
Calibrated RMSE (K)	2.40	1.57	3.31	1.11

2.5. Principal component analysis (PCA)

In order to determine the geographical direction for which one has the largest variations in surface temperature, a PCA was performed. PCA is a very well-known approach for analysing data (especially large data) to deduce meaningful conclusions about it. The principle behind PCA lies in the fact that it can mathematically determine the principal components (eigenvectors) showing the directions of the largest deviations in the data; for more information about PCA see for instance the work of Jolliffe (2002). Note that this method gives the main axes along which the variations in the data are the largest. In this analysis, it was of interest to find the direction of the land for which the temperature gradient was the largest at any given time window. Therefore, the axis that had the most variation was picked and the results were analysed accordingly. PCA was conducted for 6 four-hour time intervals.

3. Results and discussions

Three analyses were conducted on the processed image data. The first analysis represents median ST distribution at a spatial resolution of 1 km × 1 km derived from images recorded over the entire length of the field campaign. In total, 6 four-hour time intervals in LDT (00:00–04:00 LDT, 04:00–08:00 LDT, 08:00–12:00 LDT, 12:00–16:00 LDT, 16:00–20:00 LDT, and 20:00–24:00 LDT) representing ST for the entire field campaign were produced highlighting diurnal ST variation with respect to the mining facility boundary, the mine, and the tailings pond as displayed in Figure 7. Corresponding box plots representing the temperature variation of the mine and tailings pond are also included for each time interval as per Figure 8. For each survey, on average 1,910 images were used for each four-hour time interval.

The second analysis focuses on comparing the calculated ST derived from the images collected on 24 May 2018 over the 12:00–14:00 LDT time interval with respect to the MODIS MOD11A1 image recorded during the early afternoon on 24 May 2018. Three plots were created (as per Figure 9) including the ST spatial distribution map at 1 km × 1 km resolution derived from the workflow, the MOD11A1 dataset for each corresponding ST tile, and the absolute error for each tile is included.

The third analysis focuses on identifying the horizontal direction of the highest temperature variances. The direction with the highest temperature variances for each time interval was calculated from the images collected during the field campaign by completing a PCA on the data derived from each time interval. The results are presented in Figure 10.

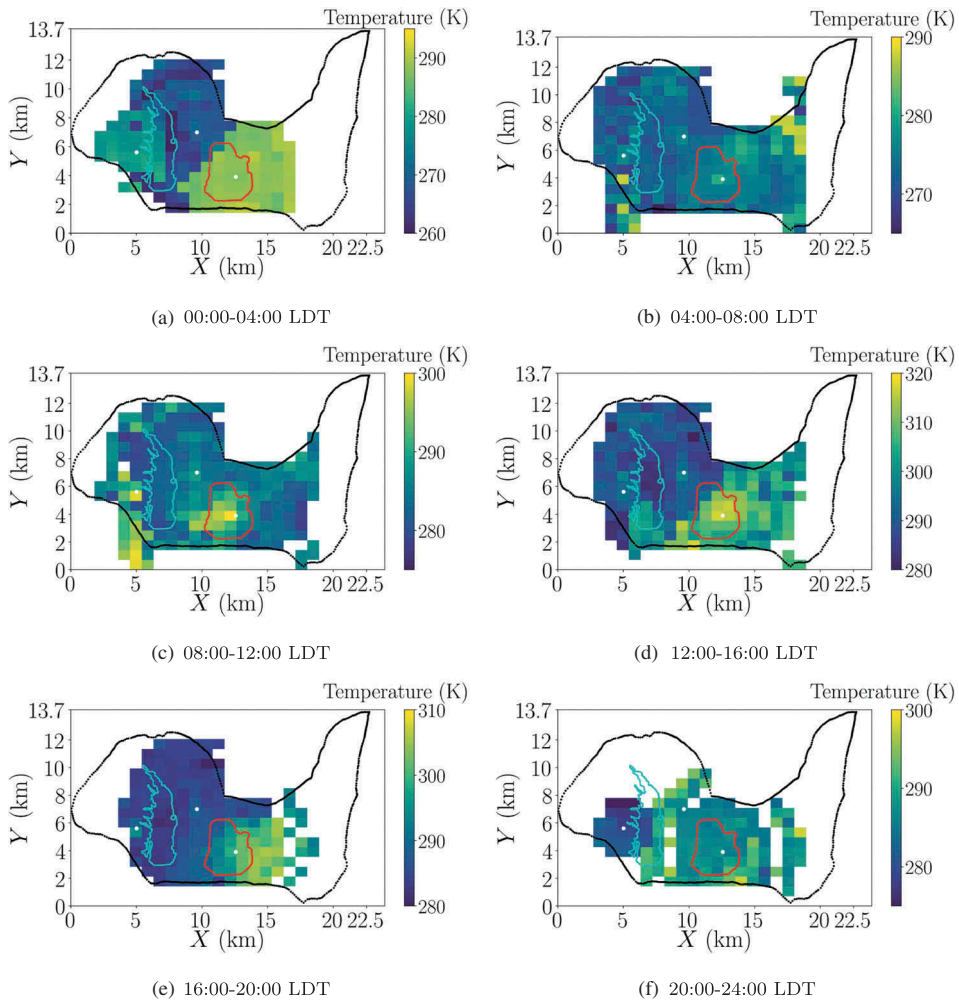


Figure 7. Median temperatures over four-hour time intervals at $1 \text{ km} \times 1 \text{ km}$ resolution; times are in Local Daylight Time (LDT).

3.1. Diurnal variation

Surface temperature maps with a spatial resolution of $1 \text{ km} \times 1 \text{ km}$ for the entire mining facility at 6 four-hour time intervals are displayed in Figure 7. These plots were created by calculating the median temperature for all data recorded within each time interval over the entire field campaign within a $1 \text{ km} \times 1 \text{ km}$ surface area (or tile). The axes represent distance in kilometres and the colour bar represents surface temperature in Kelvin.

Box plots (Figure 8) representing the surface temperature range in Kelvin of the two key geographical features of the mining facility, the mine and the tailings pond, at the corresponding 6 four-hour time intervals were created to compare ST variation diurnally. The ST values included in the box plot are located within the red and teal perimeters of the mine and tailings pond, respectively, shown in Figure 3. The black circles represent temperature values outside of the 95th and 5th percentiles. The upper

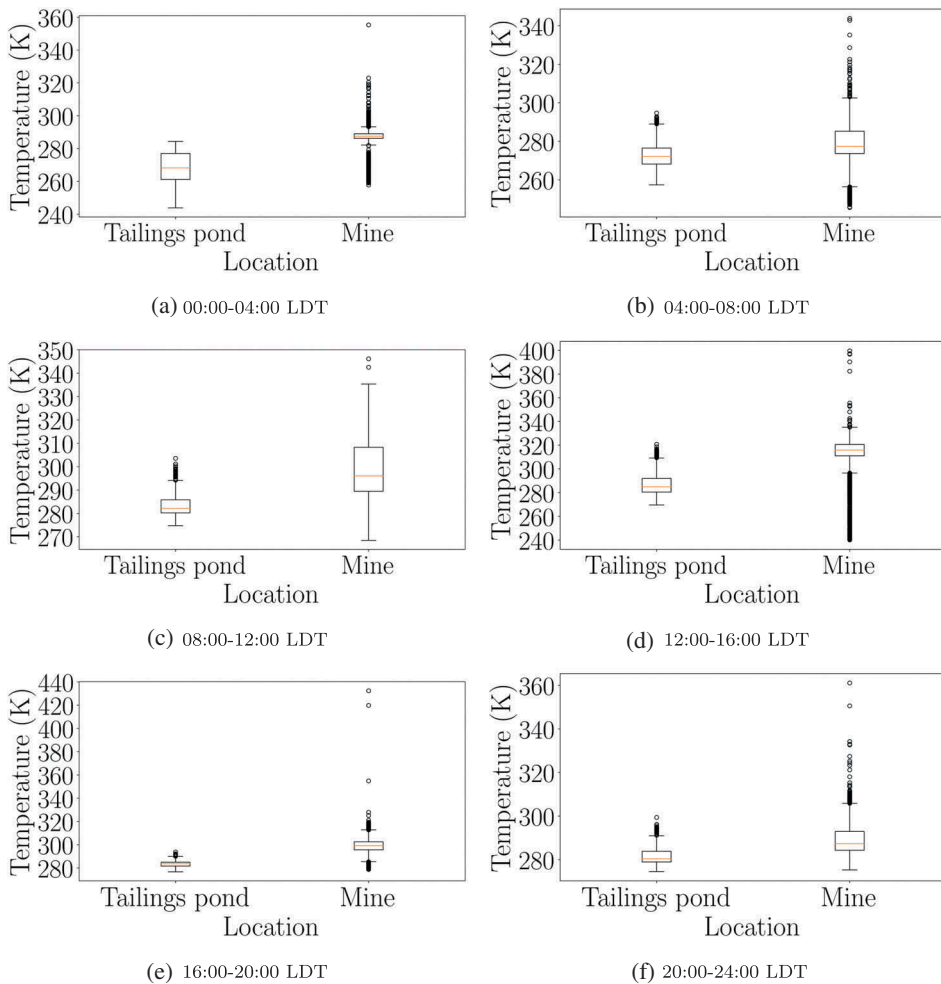


Figure 8. Box plots representing temperature distribution over four-hour time intervals for the tailings pond and mine, where the orange line is the median temperature; times are in Local Daylight Time (LDT).

black line and lower black line of the box correspond to the 95th and 5th percentiles. The middle orange line represents the median surface temperature of each geographical feature.

During the 00:00–04:00 LDT time interval, there was a distinct temperature gradient between the mine, the land west of the pond, and the pond itself. This gradient is further quantified by the corresponding box plot where the median surface temperature gradient between the two surface features was approximately 20 K.

There was a clear surface temperature gradient between the mine and the pond during the 04:00–08:00 LDT time interval. However, the magnitude of the temperature gradient between the mine and the pond was the lowest during this time period. Both the surface temperature map and the box plot display this trend as this time interval includes images captured during and after sunrise.

Over the 08:00–12:00 LDT interval, the surface temperatures of both the mine and the pond increase. Likewise, the temperature gradient between the two land surface features also grows, where the mine's ST is higher than the tailings pond ST.

During the 12:00–16:00 LDT interval, an apparent temperature gradient existed between the tailings pond and the mine. The area to the north-west of the mine had a lower surface temperature as compared to areas south and east of the mine.

The variability of surface temperatures between the mine and the pond decreased over the 16:00–20:00 LDT interval. Although a clear temperature gradient was present, the box plot displays a narrower temperature range as compared to most other time intervals.

The same temperature gradient as discussed during other time periods occurs within the 20:00–24:00 LDT period. There are a few data gaps for ST north-west of the mine as the TANAB2 was deployed less during these hours compared to other time windows. Nonetheless, the west side of the pond possesses a lower surface temperature as compared to the mine itself. The overall surface temperature magnitude for both land surface features was determined to be decreasing during this interval, after sunset.

3.2. Comparison to satellite observations

On 24 May 2018 MODIS on the Terra satellite imaged the remote mining site during the early afternoon. The TANAB2 was launched within the mine between 12:00 and 14:00 LDT on the same date. [Figure 9](#) displays the surface temperatures recorded by the thermal camera from the TANAB2, the surface temperatures recorded by MODIS from the MOD11A1 dataset, and the absolute error between the two datasets.

Absolute error with respect to MODIS temperatures on 24 May 2018 was calculated and the spatial distribution of temperature bias is displayed in [Figure 9](#). The maximum, minimum, and median absolute error were calculated to be 14.3 K, – 12.2 K, and 0.64 K, respectively. The bias and RMSE were determined to be 0.5 K and 5.45 K, respectively. Furthermore, it was noted that the absolute error increased north-west of the mine, towards the pond. This likely occurred as the TANAB2 was launched within the mine, below grade level (with respect to the mining facility), while the land elevation increases north-west of the mine towards the tailings pond. With this change in elevation, the calculated surface temperatures north-west of the mine are estimated from very oblique angle images, possibly explaining the increased error. In addition, that region contains very localized hot spots, such as pipelines, that are beyond MODIS data product resolutions to be detected by the satellite but within the resolution of the thermal images in the current method. This can also explain the discrepancy between the methods. On the other hand, the elevation of the land surface decreased south and east of the mine. This decrease is likely attributed to less oblique images and therefore lower absolute error between the two datasets. Nevertheless, the localized warm regions of surface temperatures within the mine and east of the mine recorded by MODIS were also captured from the thermal images as displayed by the surface temperature plots in [Figure 9](#).

The increase in error between the mine and the pond can be accounted for from the rapid change in topography. In this region, the bottom of the mine pit is approximately 100 m into the earth. Conversely, the area directly to the east of the pond (the levee) is the highest location of the entire site. The total change of land surface elevation between the mine and the pond is very significant and may not be fully considered by the digital

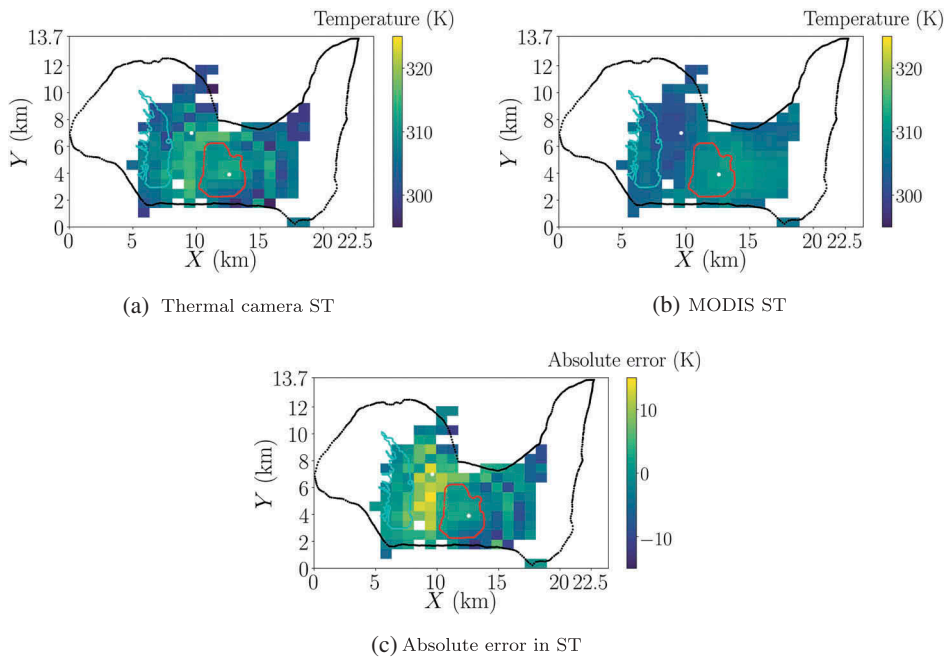


Figure 9. Comparison between the developed thermal imaging method and the MODIS MOD11A1 dataset and absolute error between the two methods; (a) median ST from 24 May 2018 12:00–14:00 LDT as recorded by the thermal camera at a $1 \text{ km} \times 1 \text{ km}$ resolution; (b) daytime temperatures captured by MODIS recorded during the early afternoon on 24 May 2018 and derived from the MOD11A1 dataset at a $1 \text{ km} \times 1 \text{ km}$ resolution; (c) absolute error between the two methods at a $1 \text{ km} \times 1 \text{ km}$ resolution; times are in Local Daylight Time (LDT).

elevation model acquired from Google Earth. Wang et al. (2017) evaluated the accuracy of elevation data provided by Google Earth for over 20,000 locations of the conterminous United States. They determined that the mean average error, RMSE, and bias of elevation was 10.72 m, 22.31 m, and 0.13 m, respectively. Based on Wang et al. (2017), Google Earth accuracy varies significantly by location. Furthermore, since the landscape of the mining facility is changing rapidly, the use of the Google Earth elevation data likely introduces further error into the method. For more accurate results, sUAS-based lidar could be a feasible solution, especially in areas where high time resolution data is required or very high resolution satellite imagery capable of creating elevation models is required (Gray et al. (2018); Akturk and Altunel (2019); Nemmaoui et al. (2019)).

Further improvement of the imaging workflow may also reduce errors. The imaging method only considers elevation profiles for the eight cardinal directions of each TANAB2 launch site. Using a Digital Elevation Model (DEM) raster and QGIS, the elevation profile for individual images could be quantified programmatically in Python. The elevation profiles for individual pixels within the image could also be quantified using this method. However, the accuracy of this method is dependent upon the accuracy and resolution of the DEM data source. Nonetheless, the accuracy of the Google Earth elevation data was deemed to be acceptable for this application.

Using oblique and very oblique images in the method may have contributed to surface temperature error even with using the corrected camera parameters R , B , O , and F .

Oblique imaging is known to affect observed surface temperatures as a function of camera pitch angle (Dugdale (2016)). Increasingly oblique imaging angles can result in a higher proportion of reflected radiation and more varied emissivity values over waterbodies (Torgersen et al. (2001); Dugdale (2016); Baker et al. (2019)). The proportion of waterbodies within the mining facility is low and even the tailings pond may not truly be representative of a pond due to byproducts introduced from the mine ore extraction process. It is known that imaging angles higher than 30° of nadir can affect surface temperature by 0.5 K (Torgersen et al. (2001); Kay et al. (2005); Dugdale (2016)). For land surfaces, James et al. (2006) recorded lava flows with $\pm 3\%$ radiative power differences. The areas with the highest temperature error were not waterbodies. Oblique images of land surfaces likely have less impact on emissivity as opposed to images of waterbodies. Nonetheless, the presence of this error source is acknowledged in this study.

Other than surface elevation variation, calculated temperature errors may have been introduced from the camera constant calibration completed in Guelph, Ontario, Canada. The surface materials at the mining site may have been different as opposed to the tested surface temperatures recorded during the calibration experiment. The difference in physical properties may have contributed to the increased minimum and maximum errors of -12.2 K and 14.3 K, respectively. However, the overall median error was calculated to be 0.64 K which is significantly below the manufacturer reported accuracy of ± 5 K and the calibrated accuracy of a FLIR Vue Pro 640 of ± 5 K (Gallardo-Saavedra, Hernández-Callejo, and Duque-Perez (2018); Kelly et al. (2019)). These elevated maximum and minimum errors may be due to highly oblique images, near horizontal, where reflected radiation can significantly impact the radiometric measurement. To avoid these errors, deploying the TANAB2 at a higher altitude would be necessary to reduce oblique imaging angles. However, this was not possible as the TANAB2 launch height was predetermined from aviation and site-specific regulations.

3.3. Principal component analysis

The result of our PCA analysis is shown in Figure 10. As can be seen, the highest surface temperature variation is along the north-west-south-east plane. Referring to Figure 3, the north-west-south-east plane intersects the mine and processing facilities to the south-east and the pond and forest to the north-west. This surface temperature variation was present in each time interval, especially during 00:00–04:00 LDT, 04:00–08:00 LDT and 16:00–20:00 LDT, where the normalized PCA horizontal directions are close to overlapping each other.

4. Conclusion and future work

A novel small Unmanned Aerial Systems (sUASs)-based and open-source thermal image processing approach was developed to directly georeference and calculate Earth surface temperature with a high spatiotemporal resolution. An uncooled thermal camera was launched on a tethered balloon during May 2018 at a remote northern Canadian mining facility. Based on the topography of the surrounding land, the camera's GPS location, the balloon altitude, and the camera's Pitch, Yaw, and Roll angles, individual pixels within each image were directly georeferenced by assigning a calculated longitude and latitude to each respective pixel. The derived imaging workflow was developed for images recorded with oblique angles relative to the land surface. The calculated land surface temperatures

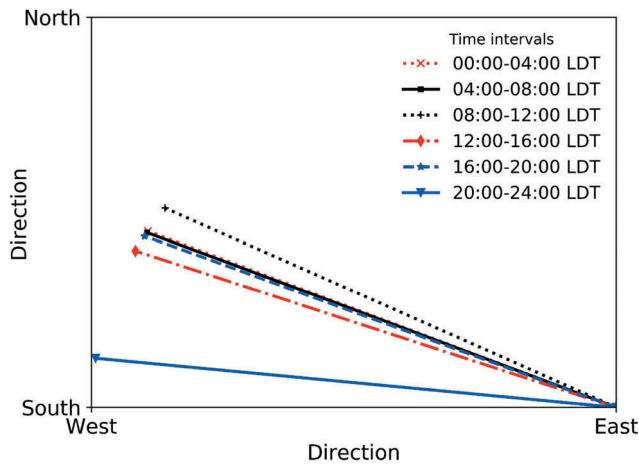


Figure 10. Representative horizontal directions encompassing the mining facility which display the largest surface temperature variation for each time interval; times are in Local Daylight Time (LDT).

accurately represented the diurnal variation of surface temperature with a high degree of spatiotemporal accuracy as compared to conventional remote sensing techniques including satellites. A comparison between a MODerate resolution Imaging Spectroradiometer (MODIS) satellite image and the results from our imaging workflow yielded a bias of 0.5 K and a Root Mean Square Error (RMSE) of 5.45 K of land surface temperatures within and surrounding the mine. A principal component analysis was conducted for each four-hour time interval and the horizontal direction with the highest surface temperature variation was the north-west-south-east direction. The principal component analysis agreed well with the diurnal surface temperature maps and the MODIS images.

This paper helps support the validity of the discussed workflow as an alternative to conventional thermal imaging devices and commercially distributed image processing software. Further verification of this workflow and its application to other land surface environments and applications, such as search and rescue operations, monitoring of urban micro-climates, and thermal plumes in waterbodies, may be considered. Likewise, additional corroboration with other satellite-based sensors and use of the thermal imaging system on other sUASs and Unmanned Aerial Vehicles (UAVs) systems could be explored in future studies.

Acknowledgements

The Tethered And Navigated Air Blimp 2 (TANAB2) was partially developed by the assistance of Denis Clement, Jason Dorssers, Katharine McNair, James Stock, Darian Vyriotes, Amanda Pinto, and Phillip Labarge. The authors thank Andrew F. Byerlay for designing and constructing the tether reel system. The authors are indebted to Steve Nyman, Chris Duiker, Peter Purvis, Manuela Racki, Jeffrey Defoe, Joanne Ryks, Ryan Smith, James Bracken, and Samantha French at the University of Guelph, who helped with the campaign logistics. Special credit is directed toward Amanda Sawlor, Datev Dodkelian, Esra Mohamed, Di Cheng, Randy Regan, Margaret Love, and Angela Vuk at the University of Guelph for administrative support. The computational platforms were set up with the assistance of Jeff Madge, Joel Best, and Matthew Kent at the University of Guelph. Technical discussions with John D. Wilson and Thomas Flesch at the University of Alberta are highly appreciated. Field support

from Alison M. Seguin (RWDI), Andrew Bellavie (RWDI), and James Ravenhill at Southern Alberta Institute of Technology (SAIT) is appreciated.

Disclosure statement

No potential conflict of interest was reported by the authors.

Funding

In-kind technical support for this work was provided by Rowan Williams Davies and Irwin Inc. (RWDI). This work was supported by the University of Guelph, Ed McBean philanthropic fund, the Discovery Grant program (401231) from the Natural Sciences and Engineering Research Council (NSERC) of Canada; Government of Ontario through the Ontario Centres of Excellence (OCE) under the Alberta-Ontario Innovation Program (AOIP) (053450); and Emission Reduction Alberta (ERA) (053498). OCE is a member of the Ontario Network of Entrepreneurs (ONE); Natural Sciences and Engineering Research Council of Canada [401231]; Ontario Centres of Excellence [053450]; Emission Reduction Alberta [053498].

ORCID

Amir A. Aliabadi  <http://orcid.org/0000-0002-1002-7536>

Data availability statement

The Atmospheric Innovations Research (AIR) Laboratory at the University of Guelph provides the source code and supporting field data via the authorisation of the data owners. For access, contact the Principal Investigator, Amir A. Aliabadi aliabadi@uoguelph.ca.

References

- Aber, J. S. 2004. "Lighter-than-air Platforms for Small-format Aerial Photography." *Transactions of the Kansas Academy of Science* 107 (1): 39-44. doi:10.1660/0022-8443(2004)107[0039:LIFSAP]2.0.CO;2.
- Akturk, E., and A. O. Altunel. 2019. "Accuracy Assessment of a Low-cost UAV Derived Digital Elevation Model (DEM) in a Highly Broken and Vegetated Terrain." *Measurement* 136: 382-386. doi:10.1016/j.measurement.2018.12.101.
- Baker, E. A., L. K. Lautz, J. M. McKenzie, and C. Aubry-Wake. 2019. "Improving the Accuracy of Time-lapse Thermal Infrared Imaging for Hydrologic Applications." *Journal of Hydrology* 571: 60-70. doi:10.1016/j.jhydrol.2019.01.053.
- Bakula, K., A. Salach, D. Z.Wziątek, W. Ostrowski, K. Górski, and Z. Kurczyński. 2017. "Evaluation of the Accuracy of Lidar Data Acquired Using a UAS for Levee Monitoring: Preliminary Results." *International Journal of Remote Sensing* 38 (8-10): 2921-2937. doi:10.1080/01431161.2016.1277044.
- Berni, J. A., P. J. Zarco-Tejada, L. Suarez, and E. Fereres. 2009. "Thermal and Narrowband Multispectral Remote Sensing for Vegetation Monitoring from an Unmanned Aerial Vehicle." *IEEE Transactions on Geoscience and Remote Sensing* 47 (3): 722-738. doi:10.1109/TGRS.2008.2010457.
- Bolanakis, D. E., K. T. Kotsis, and T. Laopoulos. 2015. "Temperature Influence on Differential Barometric Altitude Measurements." In *2015 IEEE 8th International Conference on Intelligent Data Acquisition and Advanced Computing Systems: Technology and Applications (IDAACS)*, Vol. 1, Warsaw, Poland, September 120-124. doi:10.1109/IDAACS.2015.7340711.

- Boon, M. A., A. P. Drijfhout, and S. Tesfamichael. 2017. "Comparison of a Fixed-wing and Multi-rotor UAV for Environmental Mapping Applications: A Case Study." *The International Archives of the Photogrammetry, Remote Sensing and Spatial Information Sciences XLII (2/W6)*: 47–54. doi:10.5194/isprs-archives-XLII-2-W6-47-2017.
- Budzier, H., and G. Gerlach. 2015. "Calibration of Uncooled Thermal Infrared Cameras." *Journal of Sensors and Sensor Systems* 4(1): 187–197. doi:10.5194/jsss-4-187-2015.
- Chastain, R., I. Housman, J. Goldstein, M. Finco, and K. Tenneson. 2019. "Empirical Cross Sensor Comparison of Sentinel-2A and 2B MSI, Landsat-8 OLI, and Landsat-7 ETM+ Top of Atmosphere Spectral Characteristics over the Conterminous United States." *Remote Sensing of Environment* 221: 274–285. doi:10.1016/j.rse.2018.11.012.
- Cintineo, R. M., J. A. Otkin, T. A. Jones, S. Koch, and D. J. Stensrud. 2016. "Assimilation of Synthetic GOES-R ABI Infrared Brightness Temperatures and WSR-88D Radar Observations in a High-resolution OSSE." *Monthly Weather Review* 144 (9): 3159–3180. doi:10.1175/MWR-D-15-0366.1.
- Colomina, I., and P. Molina. 2014. "Unmanned Aerial Systems for Photogrammetry and Remote Sensing: A Review." *ISPRS Journal of Photogrammetry and Remote Sensing* 92: 79–97. doi:10.1016/j.isprsjprs.2014.02.013.
- Crosson, W. L., M. Z. Al-Hamdan, S. N. J. Hemmings, and G. M. Wade. 2012. "A Daily Merged MODIS Aqua-Terra Land Surface Temperature Data Set for the Conterminous United States." *Remote Sensing of Environment* 119 (8): 315–324. doi:10.1016/j.rse.2011.12.019.
- Duffy, J. P., and K. Anderson. 2016. "A 21st-century Renaissance of Kites as Platforms for Proximal Sensing." *Progress in Physical Geography: Earth and Environment* 40 (2): 352–361. doi:10.1177/0309133316641810.
- Dugdale, S. J. 2016. "A Practitioner's Guide to Thermal Infrared Remote Sensing of Rivers and Streams: Recent Advances, Precautions and Considerations." *WIREs Water* 3: 251–268. doi:10.1002/wat2.1135.
- Eynard, D., P. Vasseur, C. Demonceaux, and V. Frémont. 2012. "Real Time UAV Altitude, Attitude and Motion Estimation from Hybrid Stereovision." *Autonomous Robots* 33 (1–2): 157–172. doi:10.1007/s10514-012-9285-0.
- Fang, L., X. Zhan, C. R. Hain, J. Yin, J. Liu, M. A. Schull. 2018. "An Assessment of the Impact of Land Thermal Infrared Observation on Regional Weather Forecasts Using Two Different Data Assimilation Approaches." *Remote Sensing-Basel* 10 (4): 625. doi:10.3390/rs10040625.
- FLIR-sUAS. 2016. *Radiometric temperature measurement*. Technical Report. FLIR Systems.
- FLIR-Systems. 2012. *The ultimate infrared handbook for R&D professionals*. FLIR Systems.
- Gallardo-Saavedra, S., L. Hernández-Callejo, and O. Duque-Perez. 2018. "Technological Review of the Instrumentation Used in Aerial Thermographic Inspection of Photovoltaic Plants." *Renewable and Sustainable Energy Reviews* 93: 566–579. doi:10.1016/j.rser.2018.05.027.
- Gémes, O., Z. Tobak, and B. van Leeuwen. 2016. "Satellite Based Analysis of Surface Urban Heat Island Intensity." *Journal of Environmental Geography* 9 (1–2): 23–30. doi:10.1515/jengeo-2016-0004.
- Gray, P. C., J. T. Ridge, S. K. Poulin, A. C. Seymour, A. M. Schwantes, J. J. Swenson, and D. W. Johnston. 2018. "Integrating Drone Imagery into High Resolution Satellite Remote Sensing Assessments of Estuarine Environments." *Remote Sensing-Basel* 10 (8): 1257. doi:10.3390/rs10081257.
- Hardin, P. J., V. Lulla, and R. R. Jensen. 2019. "Small Unmanned Aerial Systems (sUAS) for Environmental Remote Sensing: Challenges and Opportunities Revisited." *GIScience & Remote Sensing* 56 (2): 309–322. doi:10.1080/15481603.2018.1510088.
- Hopkinson, C., J. Barlow, M. Demuth, and J. Pomeroy. 2010. "Mapping Changing Temperature Patterns over a Glacial Moraine Using Oblique Thermal Imagery and Lidar." *Canadian Journal of Remote Sensing* 36 (Suppl. 2): S257–S265. doi:10.5589/m10-053.
- Horrocks, L. A., B. Candy, T. J. Nightingale, R. W. Saunders, A. O'Carroll, and A. R. Harris. 2003. "Parameterizations of the Ocean Skin Effect and Implications for Satellite-based Measurement of Sea-surface Temperature." *Journal of Geophysical Research: Oceans* 108 (C3): 3096. doi:10.1029/2002JC001503.
- Horton, T. W., A. Oline, N. Hauser, T. M. Khan, A. Laute, A. Stoller, K. Tison, and P. Zawar-Reza. 2017. "Thermal Imaging and Biometrical Thermography of Humpback Whales." *Frontiers in Marine Science* 4: 424. doi:10.3389/fmars.2017.00424.

- Inamdar, A. K., A. French, S. Hook, G. Vaughan, and W. Lueckert. 2008. "Land Surface Temperature Retrieval at High Spatial and Temporal Resolutions over the Southwestern United States." *Journal of Geophysical Research: Atmospheres* 113 (D7): 1–18. doi:10.1029/2007JD009048.
- James, M. R., S. Robson, H. Pinkerton, and M. Ball. 2006. "Oblique Photogrammetry with Visible and Thermal Images of Active Lava Flows." *Bulletin of Volcanology* 69 (1): 105–108. doi:10.1007/s00445-006-0062-9.
- Jolliffe, I. T. 2002. *Principal Component Analysis*. 2nd ed. New York: Springer-Verlag.
- Kawai, Y., and A. Wada. 2007. "Diurnal Sea Surface Temperature Variation and Its Impact on the Atmosphere and Ocean: A Review." *Journal of Oceanography* 63 (5): 721–744. doi:10.1007/s10872-007-0063-0.
- Kay, J. E., S. K. Kampf, R. N. Handcock, K. A. Cherkauer, A. R. Gillespie, and S. J. Burges. 2005. "Accuracy of Lake and Stream Temperatures Estimated from Thermal Infrared Images." *Journal of the American Water Resources Association* 41 (5): 1161–1175. doi:10.1111/j.1752-1688.2005.tb03791.x.
- Kelly, J., N. Kljun, P.-O. Olsson, L. Mihai, B. Liljeblad, P. Weslien, L. Klemedtsson, and L. Eklundh. 2019. "Challenges and Best Practices for Deriving Temperature Data from an Uncalibrated UAV Thermal Infrared Camera." *Remote Sensing-Basel* 11(5): 567. doi:10.3390/rs11050567.
- Klemas, V. V. 2015. "Coastal and Environmental Remote Sensing from Unmanned Aerial Vehicles: An Overview." *Journal of Coastal Research* 31 (5): 1260–1267. doi:10.2112/JCOASTRES-D-15-00005.1.
- Kolodochka, A. A. 2003. "Schemes of Profile Models of Heat and Mass Transfer in Large Lakes." *Water Resources* 30 (1): 34–41. doi:10.1023/A:1022095516371.
- Ku, H. H. 1966. "Notes on the Use of Propagation of Error Formulas." *Journal of Research of the National Bureau of Standards Section C: Engineering and Instrumentation* 70 (4): 263.
- Kumar, A. 2014. "Long Term (2003-2012) Spatio-temporal MODIS (Terra/Aqua Level 3) Derived Climatic Variations of Aerosol Optical Depth and Cloud Properties over a Semi Arid Urban Tropical Region of Northern India." *Atmospheric Environment* 83: 291–300. doi:10.1016/j.atmosenv.2013.10.030.
- Lin, D., H.-G. Maas, P. Westfeld, H. Budzier, and G. Gerlach. 2018. "An Advanced Radiometric Calibration Approach for Uncooled Thermal Cameras." *The Photogrammetric Record* 33 (161): 30–48. doi:10.1111/phor.12216.
- Liu, L., C. Li, Y. Lei, J. Yin, and J. Zhao. 2017. "Volcanic Ash Cloud Detection from MODIS Image Based on CPIWS Method." *Acta Geophysica* 65 (1): 151–163. doi:10.1007/s11600-017-0013-1.
- Malbêteau, Y., S. Parkes, B. Aragon, J. Rosas, and M. F. McCabe. 2018. "Capturing the Diurnal Cycle of Land Surface Temperature Using an Unmanned Aerial Vehicle." *Remote Sensing-Basel* 10 (9): 1407. doi:10.3390/rs10091407.
- Mathew, A., S. Khandelwal, and N. Kaul. 2018. "Analysis of Diurnal Surface Temperature Variations for the Assessment of surface Urban Heat Island Effect over Indian Cities." *Energy and Buildings* 159: 271–295. doi:10.1016/j.enbuild.2017.10.062.
- Mildrexler, D. J., M. Zhao, and S. W. Running. 2011. "Satellite Finds Highest Land Skin Temperatures on Earth." *Bulletin of the American Meteorological Society* 92 (7): 855–860. doi:10.1175/2011BAMS3067.1.
- Moen, R., J. Pastor, and Y. Cohen. 1997. "Accuracy of GPS Telemetry Collar Locations with Differential Correction." *The Journal of Wildlife Management* 61 (2): 530–539. doi:10.2307/3802612.
- Moukoma, S., and P. D. Blanken. 2016. "Remote Sensing of the North American Laurentian Great Lakes' Surface Temperature." *Remote Sensing-Basel* 8 (4): 286. doi:10.3390/rs8040286.
- Nemmaoui, A., F. J. Aguilar, M. A. Aguilar, and R. Qin. 2019. "DSM and DTM Generation from VHR Satellite Stereo Imagery over Plastic Covered Greenhouse Areas." *Computers and Electronics in Agriculture* 164: 104903. doi:10.1016/j.compag.2019.104903.
- Olbrycht, R., and Więcek. 2015. "New Approach to Thermal Drift Correction in Microbolometer Thermal Cameras." *Quantitative InfraRed Thermography Journal* 12 (2): 184–195. doi:10.1080/17686733.2015.1055675.
- Padró, J.-C., F.-J. Muñoz, J. Planas, and X. Pons. 2019. "Comparison of Four UAV Georeferencing Methods for Environmental Monitoring Purposes Focusing on the Combined Use with Airborne and Satellite Remote Sensing Platforms." *International Journal of Applied Earth Observation and Geoinformation* 75: 130–140. doi:10.1016/j.jag.2018.10.018.

- Patel, N. R. 2006. "Investigating Relations between Satellite Derived Land Surface Parameters and Meteorological Variables." *Geocarto International* 21 (3): 47–53. doi:10.1080/10106040608542392.
- Puliti, S., H. O. Ørka, T. Gobakken, and E. Næsset. 2015. "Inventory of Small Forest Areas Using an Unmanned Aerial System." *Remote Sensing-Basel* 7 (8): 9632–9654. doi:10.3390/rs70809632.
- Rahaghi, A. I., U. Lemmin, D. Sage, and D. A. Barry. 2019. "Achieving High-resolution Thermal Imagery in Low-contrast Lake Surface Waters by Aerial Remote Sensing and Image Registration." *Remote Sensing of Environment* 221: 773–783. doi:10.1016/j.rse.2018.12.018.
- Rahaman, K. R., Q. K. Hassan, and E. H. Chowdhury. 2018. "Quantification of Local Warming Trend: A Remote Sensing-based Approach." *PloS One* 13 (5): e0196882. doi:10.1371/journal.pone.0196882.
- Rankin, A. M., and E. W. Wolff. 2002. "Aerosol Profiling Using a Tethered Balloon in Coastal Antarctica." *Journal of Atmospheric and Oceanic Technology* 19 (12): 1978–1985. doi:10.1175/1520-0426(2002)019<1978:APUATB>2.0.CO;2.
- Reichle, R. H., S. V. Kumar, S. P. P. Mahanama, R. D. Koster, and Q. Liu. 2010. "Assimilation of Satellite-derived Skin Temperature Observations into Land Surface Models." *Journal of Hydrometeorology* 11: 1103–1122. doi:10.1175/2010JHM1262.1.
- Reintsma, K. M., P. C. McGowan, C. Callahan, T. Collier, D. Gray, J. D. Sullivan, and D. J. Prosser. 2018. "Preliminary Evaluation of Behavioral Response of Nesting Waterbirds to Small Unmanned Aircraft Flight." *Waterbirds* 41 (3): 326–331. doi:10.1675/063.041.0314.
- Ren, L., M. Castillo-Effen, H. Yu, E. Johnson, Y. Yoon, N. Takuma, and C. A. Ippolito. 2017. "Small Unmanned Aircraft System (Suas) Categorization Framework for Low Altitude Traffic Services." In *2017 IEEE/AIAA 36th Digital Avionics Systems Conference (DASC)*, St. Petersburg, FL, USA, September. doi:10.1109/DASC.2017.8101996.
- Ribeiro-Gomes, K., D. Hernández-López, J. F. Ortega, R. Ballesteros, T. Poblete, and M.A. Moreno. 2017. "Uncooled Thermal Camera Calibration and Optimization of the Photogrammetry Process for UAV Applications in Agriculture." *Sensors-Basel* 17 (10): 2173. doi:10.3390/s17102173.
- Schmidt, J., I. S. Evans, and J. Brinkmann. 2003. "Comparison of Polynomial Models for Land Surface Curvature Calculation." *International Journal of Geographical Information Science* 17 (8): 797–814. doi:10.1080/13658810310001596058.
- Schmit, T. J., P. Griffith, M. M. Gunshor, J. M. Daniels, S. J. Goodman and W. J. Lebar. 2017. "A Closer Look at the ABI on the GOES-R Series." *Bulletin of the American Meteorological Society* 98 (4): 681–698. doi:10.1175/BAMS-D-15-00230.1.
- Sheng, H., H. Chao, C. Coopmans, J. Han, M. McKee, and Y. Chen. 2010. "Low-cost UAV-based Thermal Infrared Remote Sensing: Platform, Calibration and Applications." In *Proceedings of 2010 IEEE/ASME International Conference on Mechatronic and Embedded Systems and Applications*, 38–43, Qingdao, China. doi:10.1109/MESA.2010.5552031.
- Smith, G. M., and E. J. Milton. 1999. "The Use of the Empirical Line Method to Calibrate Remotely Sensed Data to Reflectance." *International Journal of Remote Sensing* 20 (13): 2653–2662. doi:10.1080/014311699211994.
- Stöcker, C., F. Nex, M. Koeva, and M. Gerke. 2017. "Quality Assessment of Combined IMU/GNSS Data for Direct Georeferencing in the Context of UAV-based Mapping." *The International Archives of the Photogrammetry, Remote Sensing and Spatial Information Sciences XLII (2/W6)*: 355–361. doi:10.5194/isprs-archives-XLII-2-W6-355-2017.
- Stull, R. B. 2015. *Practical Meteorology: An Algebra-based Survey of Atmospheric Science*. Univ. of British Columbia.
- Tomlinson, C. J., L. Chapman, J. E. Thornes and C. Baker. 2011. "Remote Sensing Land Surface Temperature for Meteorology and Climatology: A Review." *Meteorological Applications* 18 (3): 296–306. doi:10.1002/met.287.
- Torgersen, C. E., R. N. Faux, B. A. McIntosh, N. J. Poage, and D. J. Norton. 2001. "Airborne Thermal Remote Sensing for Water Temperature Assessment in Rivers and Streams." *Remote Sensing of Environment* 76 (3): 386–398. doi:10.1016/S0034-4257(01)00186-9.

- Torres-Rua, A. 2017. "Vicarious Calibration of sUAS Microbolometer Temperature Imagery for Estimation of Radiometric Land Surface temperature." *Sensors-Basel* 17 (7): 1499. doi:10.3390/s17071499.
- Turner, D., A. Lucieer, and L. Wallace. 2014. "Direct Georeferencing of Ultrahigh-resolution UAV Imagery." *IEEE Transactions on Geoscience and Remote Sensing* 52 (5): 2738–2745. doi:10.1109/TGRS.2013.2265295.
- Usamentiaga, R., P. Venegas, J. Guerediaga, L. Vega, J. Molleda, and F. G. Bulnes. 2014. "Infrared Thermography for Temperature Measurement and Non-destructive Testing." *Sensors-Basel* 14 (7): 12305–12348. doi:10.3390/s140712305.
- van der Meer, F. 2018. "Near-infrared Laboratory Spectroscopy of Mineral Chemistry: A Review." *International Journal of Applied Earth Observation and Geoinformation* 65: 71–78. doi:10.1016/j.jag.2017.10.004.
- Verykokou, S., and C. Ioannidis. 2018. "Oblique Aerial Images: A Review Focusing on Georeferencing Procedures." *International Journal of Remote Sensing* 39 (11): 3452–3496. doi:10.1080/01431161.2018.1444294.
- Vierling, L. A., M. Fersdahl, X. Chen, L. Zhengpeng, and P. Zimmerman. 2006. "The Short Wave Aerostat-Mounted Imager (SWAMI): A Novel Platform for Acquiring Remotely Sensed Data from A Tethered Balloon." *Remote Sensing of Environment* 103 (3): 255–264. doi:10.1016/j.rse.2005.01.021.
- von Bueren, S. K., A. Burkart, A. Hueni, U. Rascher, M. P. Tuohy, and I. J. Yule. 2015. "Deploying Four Optical UAV-based Sensors over Grassland: Challenges and Limitations." *Biogeosciences* 12 (1): 163–175. doi:10.5194/bg-12-163-2015.
- Wang, K., Z. Wan, P. Wang, M. Sparrow, J. Liu, X. Zhou, and S. Haginoya. 2005. "Estimation of Surface Long Wave Radiation and Broadband Emissivity Using Moderate Resolution Imaging Spectroradiometer (MODIS) Land Surface Temperature/emissivity Products." *Journal of Geophysical Research: Atmospheres* 110 (11). doi:10.1029/2004JD005566.
- Wang, Y., Y. Zou, K. Henrickson, Y. Wang, J. Tang, and B.-J. Park. 2017. "Google Earth Elevation Data Extraction and Accuracy Assessment for Transportation Applications." *PloS One* 12 (4): 1–17. doi:10.1371/journal.pone.0175756.
- Whitehead, K., C. H. Hugenholtz, S. Myshak, O. Brown, A. LeClair, and A. Tamminga. 2014. "Remote Sensing of the Environment with Small Unmanned Aircraft Systems (Uass), Part 2: Scientific and Commercial Applications." *Journal of Unmanned Vehicle Systems*, 3: 86–102. doi:10.1139/juvs-2014-0007.
- Zakšek, K., and K. Oštir. 2012. "Downscaling Land Surface Temperature for Urban Heat Island Diurnal Cycle Analysis." *Remote Sensing of Environment* 117: 114–124. doi:10.1016/j.rse.2011.05.027.
- Zeise, B., S. P. Kleinschmidt, and B. Wagner. 2015. "Improving the Interpretation of Thermal Images with the Aid of Emissivity's Angular Dependency." In *2015 IEEE International Symposium on Safety, Security and Rescue Robotics (SSRR)*, 1–8, West Lafayette, IN, USA. doi:10.1109/SSRR.2015.7442950.
- Zhang, X. H., F. Guo, and X. X. Li. 2012. "A Novel Stop&Go GPS Precise Point Positioning (PPP) Method and Its Application in Geophysical Exploration and Prospecting." *Survey Review* 44 (327): 251–255. doi:10.1179/1752270611Y.0000000016.